Earth System
Science
Data

Open Access

Measurements of water droplet size distributions in a turbulent wind tunnel

Wiebke Frey[1], **Silvio Schmalfuß**[2], **Frank Stratmann**[2], **and Dennis Niedermeier**[2]

[1]Meteorology and Air Quality Group, Wageningen University, Wageningen, the Netherlands
[2]Leibniz Institute for Tropospheric Research (TROPOS), Leipzig, Germany

Correspondence: Wiebke Frey (wiebke.frey@wur.nl)

Abstract. In order to study the behaviour of cloud droplets at the cloud-clear interface, the "Solving The Entrainment Puzzle" (STEP) project examined a droplet stream in the Turbulent Leipzig Aerosol Cloud Interaction Simulator (LACIS-T). LACIS-T comprises two particle free air streams, that are turbulently mixed, and during the experiment one air stream was resembling in-cloud conditions, whereas the other air stream was set to out-of-cloud conditions. A droplet stream was injected by a droplet generator into the mixing plane of the two air streams. Droplet size distributions were observed with a phase Doppler anemometer at various levels in the measurement section of LACIS-T, corresponding to different residence times of the droplets in the turbulent environment. Additionally, observations were made using different flow speeds in the two air streams to create shear flows in the wind tunnel. The experiment was accompanied by computational fluid dynamics simulations to provide a full 3D representation of meteorological fields and turbulence parameters. This manuscript provides a description of the laboratory settings and instrumentation, the experimental design, the simulations, and a general overview of the data. We invite the scientific community for joint data analysis and numerical studies using the data which is freely available from the Eurochamp Data Centre, see Table 2 in the Data availability section for details.

1 Introduction

To understand how clouds develop, it is necessary to understand the processes happening at the cloud-clear interface: multiple studies try to decipher how cloud particles react to cloud free air mixed into the cloud (entrainment; e.g. Bera et al., 2016; Chandrakar et al., 2021; Lehmann et al., 2009; Lim and Hoffmann, 2023; Wang et al., 2024). Possibilities range from dilution of the cloud, i.e. reducing the number of cloud droplets while leaving their size unchanged (extreme inhomogeneous mixing) to a scenario where the turbulent mixing proceeds fast compared to the time that the cloud droplets need to react to the new environmental conditions (humidity and temperature), thus all droplets evaporate to some extent but none completely and thus, the whole size distribution shifts towards smaller sizes (extreme homogeneous mixing). Mixing processes in clouds have been identified to play an important role in cloud climate feedbacks, being re-

sponsible for large parts of the spread in climate sensitivity estimates (Klocke et al., 2011; Sherwood et al., 2014; Klein and Hall, 2015). These mixing processes are facilitated by turbulently driven eddies, which raises the additional question, how exactly entrainment and turbulence are linked. The physical understanding of entrainment remains low, as e.g. Lu et al. (2018) emphasise by pointing out the contradictions in entrainment parameterisations. Current knowledge assumes, that mixing on larger scales is inhomogeneous, while it is homogeneous on the small scales (e.g. Lehmann et al., 2009; Lim and Hoffmann, 2023). What exactly large and small means, and thus, the exact scale of transition from homogeneous to inhomogeneous mixing is hard to establish: in situ aircraft measurements are not highly resolved enough in space and time, while in Large Eddy Simulations (LES), that typically simulate whole clouds or cloud fields, the transition happens on the subgrid scale (SGS). Direct Numerical Simulations (DNS) are highly resolved, but are too compu-

tationally costly to be run over large enough domains. Helicopter borne in situ measurements seem to provide a good option, but come with their very own limitations (Siebert et al., 2006). Similarly, tethered balloon systems using helikites like the CloudKite (Schlenczek et al., 2025; Stevens et al., 2021) can provide a platform for highly resolved observations. However, as ground-anchored systems, they cannot actively target regions of interest horizontally and are limited by payload and maximum ceiling. Holographic systems aboard aircraft, which can sample small volumes of droplets at one time, might circumvent the scale issue in aircraft measurements to some extent (e.g. Desai et al., 2021). Allwayin et al. (2024) inferred from holographic measurements that the local characteristics of microphysical properties deviate from the cloud scale (or cloud transect) average microphysical properties. Still, these measurements are only able to capture snapshots and cannot observe the time evolution of the cloud. The difficulty of studying mixing processes from field observations arises from the fact that not only the spatial scales are important but also the temporal scales: It does matter whether the turbulent mixing is fast compared to the cloud mircophysical reaction time or slow. A further fact that complicates the picture is coexistence of eddies with different length and time scales acting simultaneously (Lehmann et al., 2009; Kumar et al., 2013). On the modelling side, a promising approach to study mixing is to use SGS models combined with Lagrangian cloud models, using superdroplets (e.g. Hoffmann and Feingold, 2019; Chandrakar et al., 2021; Lim and Hoffmann, 2023). More recently, i.e. in the past decade, laboratory experiments combining cloud chambers with well-characterised turbulence became operational (Π-Chamber and LACIS-T; Chang et al., 2016; Niedermeier et al., 2020). These chambers provide the opportunity to study turbulent cloud mixing in a controlled environment, additionally allowing for assessing relevant time and lengths scales, at least to some extent. Experiments in the Π-Chamber attributed seemingly conflicting results in terms of mixing to local versus global scales: mixing was found to be inhomogeneous locally and homogeneous globally (Yeom et al., 2023). In more general, cloud particle-turbulence interactions are discussed e.g. in the review papers by Shaw (2003), Devenish et al. (2012), and Grabowski and Wang (2013). We would like to refer the interested reader to those publications, and only briefly describe further impacts of entrainment(-mixing) and turbulence on cloud droplet size distributions in the following: Due to the small scale fluctuations in the background meteorological fields, cloud particles experience slightly different conditions, thus having different growth histories (e.g. Lasher-Trapp et al., 2005; Tölle and Krueger, 2014; Niedermeier et al., 2025). This is supposed to lead to a broadening in the size distributions, especially in combination with large-eddy hopping (Grabowski and Wang, 2013). Sardina et al. (2015) found that larger scale turbulent fluctuations determine the rate of size distribution broadening. Also aerosol concentrations have been found to impact

the turbulent cloud size distribution broadening (Chandrakar et al., 2016). Fluctuations in the wind field will impact the relative velocities of cloud droplets and potentially increase their chance of colliding (Khain et al., 2007; Chen et al., 2018). This is particularly important for same or similar sized droplets, which under a gravitational collision and coalescence viewpoint would not collide. Therefore, turbulence is thought to have an enhancing effect on collision and coalescence (Ayala et al., 2008; Onishi and Seifert, 2016). In addition, turbulence can lead to cloud voids (i.e. tube like holes in the cloud with radius of a few centimeters; Karpińska et al., 2019) or to cloud droplet clustering (Vaillancourt et al., 2002; Saw and Meng, 2022; D'Alessandro and McFarquhar, 2023). Both mechanisms are affecting the chances of droplet collisions and thus, droplet growth by collision and coalescence.

In order to advance our understanding in cloud microphysics-turbulence interactions, Morrison et al. (2020) argue that greater emphasis should be given to laboratory work. Therefore, the "Solving The Entrainment Puzzle" (STEP) project was aiming at gaining a better understanding of how entrainment affects cloud droplet size distributions, using the Turbulent Leipzig Aerosol Cloud Interaction Simulator (LACIS-T; Niedermeier et al., 2020), in combination with computational fluid dynamics simulations. This paper describes the setup and procedure of the main set of measurements with their corresponding simulations, and the data set which can be openly accessed from the Eurochamp Data Centre. In addition, we provide some examples for potential studies that could use these data.
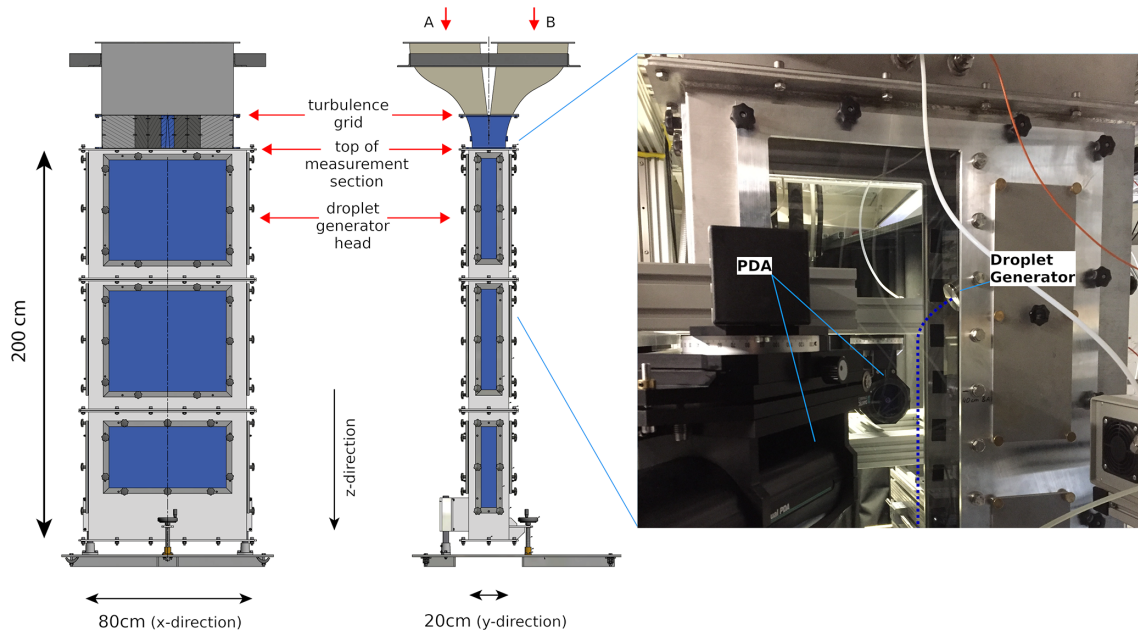
2 Measurement setup

This section describes the measurement setup, i.e. the turbulent wind tunnel and the general measurements, the droplet generation, and the droplet measurements.

2.1 Wind tunnel

LACIS-T is a moist air, closed loop, Göttingen type wind tunnel, that allows to study the interactions of cloud microphysics and turbulence. A detailed description is given in Niedermeier et al. (2020), so we only repeat the major characteristics which are important for this study. A main feature of the wind tunnel is that it comprises two air streams that can be controlled separately in terms of temperature, humidity, and flow speed. The accuracy of the heat exchangers (for the temperature settings) and the humidification system (for dew point settings) is monitored by Pt100 resistance thermometers and dew point mirrors, with accuracies of $\pm 0.0300\,°C + 0.005 \times T$ and $\pm 0.1\,K$, respectively. The two air streams (stream A and stream B) are combined at the beginning of the measurement section, depicted in Fig. 1.

The flow speed is measured by a vane anemometer before inclusion of the droplet generator, with an uncertainty of $\pm(\leq 1.5\,\%$ (of measured value) $+ 0.03\,m\,s^{-1})$. Turbulence

Figure 1. Sketch of the LACIS-T measurement section, showing the x–z perspective on the left (with z pointing downward), and y–z perspective in the right sketch (© by Ingenieurbüro Mathias Lippold, VDI; TROPOS). The x and y origins are located in the middle of the measurement section. The picture on the right shows the upper part of the measurement section, with the PDA instrument sending and receiving optics to the left and the head of the droplet generator visible on the right side of the window. The droplet stream is indicated by the dark blue dash.

is induced by a passive square-mesh grid which is located just upstream the measurement section, 20 cm above where the two air streams combine. The mesh length of the grid is 1.9 cm with a rod diameter of 4 mm and the grid creates a blockage of 30 %.

2.2 Droplet generation

For the generation of cloud droplets, a Monodisperse Droplet Generator (MDG, model 1530, MSG corporation) is used. The droplet generator head is installed inside the measurement section, in a way that the droplets are injected into the mixing plane. The droplets exit the head about 34.5 cm below the top of the measurement section with a x–z trajectory to avoid a strong blockage of the flow by the MDG head. However, an influence of the generator head geometry on the air flow cannot be ruled out and is likely. The angle between the particle stream exiting the MDG head and the x-vector is about 20°. After travelling 5 cm downwards (z-direction) the approximate middle of the particle stream has reached an x-position that diverges 35 to 40 mm from the origin at the droplet generator, and mostly also stays there further downstream. On two consecutive days the droplet stream diverged a bit less/more, i.e. on 21 and 22 February 2022, which might be related to a change in weather, as can also be noted in the laboratory conditions (Appendix B, cf. Table B1). The droplet generator is operated using purified water with a liquid water flow (Q) of 2 mL h^{-1} and a frequency of 220 kHz.

The inlet air and flow focussing air pressure were set in a range of 12.0 to 12.2 psi and 2.81 to 2.83 psi, respectively (i.e. 827.4 to 841.2 mbar and 193.7 to 195.1 mbar). The flow focussing air pressure was later changed to 3.15 to 3.18 psi (217.2 to 219.3 mbar) after some additional testing of the droplet generator. This would still provide a droplet stream with a comparable size distribution of droplets generated by the MDG for all measurements, while the MDG itself operated a bit more stable. The resulting initial and final size distributions were measured as close as possible to the droplet generator head ($z = 0$ cm), an example of resulting size distributions for several measurement days is displayed in Fig. 2.

2.3 Droplet measurements: PDA on moving frame

The detection of cloud particles is performed by a 3D Dual Phase Doppler Anemometer (PDA, Dantec Dynamics) system. The PDA uses the phase shift observed by two detectors, receiving scattered light from particles crossing the intersection volume of two laser beams, which is proportional to the particle diameter, to measure the sizes of individual particles, and the observed Doppler frequency to calculate the particle velocity. The PDA system used in this study was set up for observing water droplets with sizes up to 48.4 µm. The lower size limit is given by two times the laser wave length (which for the PDA is 532 nm), however, the small sizes have been found to be sized incorrectly, and therefore sizes below 5 µm are not considered. The transmitting and receiving optics of
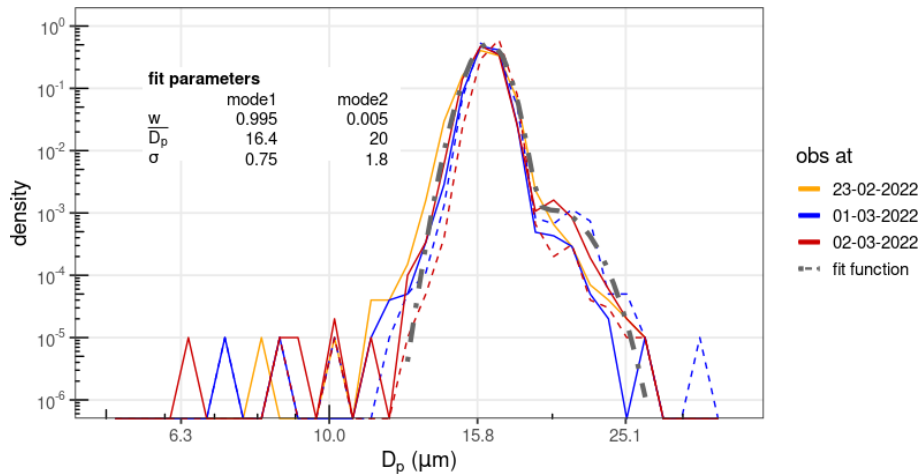
Figure 2. Initial and final size distributions (solid and dashed lines, respectively) at $z = 0$ cm for several measurement days. The broad grey dot-dashed line represents the fit function. Fit parameters (as used for Eq. 1, see Sect. 5) are specified in the plot as well.

the PDA system are installed on a traverse outside the measurement section, thus, it provides non-intrusive measurements of the particles and the sample volume can be moved in all three directions (x/y in horizontal and z in the vertical), allowing for droplet observations at various positions within the measurement section of LACIS-T. The windows of the LACIS-T measurement section are made of borosilicate glass for a high transmissivity of the laser wavelengths. The PDA is operated in a forward scattering mode.

3   Experiment design

The conditions in LACIS-T during all experiments are set to resemble in-cloud conditions in stream A and out-of-cloud conditions in stream B, which are warmer and dryer. The temperature and dew point temperature in stream A are set to 10 and 9.9 °C and to 16 and 5 °C in stream B, respectively. The flow rate in stream A is set to 4.5 m³ min⁻¹ which translates to a flow speed of 1.31 m s⁻¹, and is varied in stream B in order to create a shear flow. The flow rate in stream B is set to 4.5, 3.0, or 1.5 m³ min⁻¹, i.e. 1.31, 1.0, or 0.67 m s⁻¹. That results in a shear flow with a maximum velocity difference of 0.64 m s⁻¹ over the very short distance of the mixing plane, or if considering the middle of both streams over 10 cm. Compared to observed velocity differences as for example in marine stratocumulus as in Siebert et al. (2010, e.g. their Fig. 4) this might seem rather small, however, the larger differences in velocities during field observations were also observed over larger distances. Therefore, we believe that shear rates selected in LACIS-T should lead to well observable effects, as when extrapolated to larger distances they would result in higher velocity differences. After sufficient start up time of LACIS-T to allow the set conditions (i.e. temperatures, dew points, flow speeds) to stabilise, each experiment started with a measurement of the droplet size distribution as close to the MDG head as possible, to retrieve the initial size distribution. The droplet generator was given a spin up time of at least half an hour as well to ensure a stable droplet size distribution. This was particularly necessary when it had been flushed with isopropanol before, to assure that the droplets contain water only. The level of the first measurement is denoted $z = 0$ cm. Subsequently, the traverse is moved downwards to allow taking droplet measurements at $z = 5$ cm, $z = 20$ cm, $z = 50$ cm, and $z = 80$ cm (positive z means below droplet generator). Figure 3 gives an impression of the change of the droplet stream on the different levels, by showing pictures of the droplet stream that is illuminated by the PDA lasers. It is clearly visible, how the stream broadens with time (distance from droplet generator), and also how variable the droplet stream can be, as seen on the right side with the two pictures of the droplet stream at $z = 80$ cm.

The x- and y-positions of the traverse are adjusted in a way that the PDA measures in the approximate middle of the droplet stream for any of the $z > 0$ cm levels. After finishing the final size distribution measurement at $z = 80$ cm, the PDA is moved up to the first position at $z = 0$ cm to check for potential drift in the initial size distribution of the droplet stream (cf. Fig. 2). The sample time for the PDA is 300 or 600 s for $z = 5$ cm and $z = 20$ cm, and 600 s for $z = 50$ cm and $z = 80$ cm, as the particle number concentrations drop due to the broadening of the droplet stream. At the droplet generator head ($z = 0$ cm) it samples until reaching 100 000 particles, which takes a couple of seconds. The exact sample times are specified in Table A1.

4   Measurement data

This section includes a description of the general data observed during the experiments, as well as the specific data
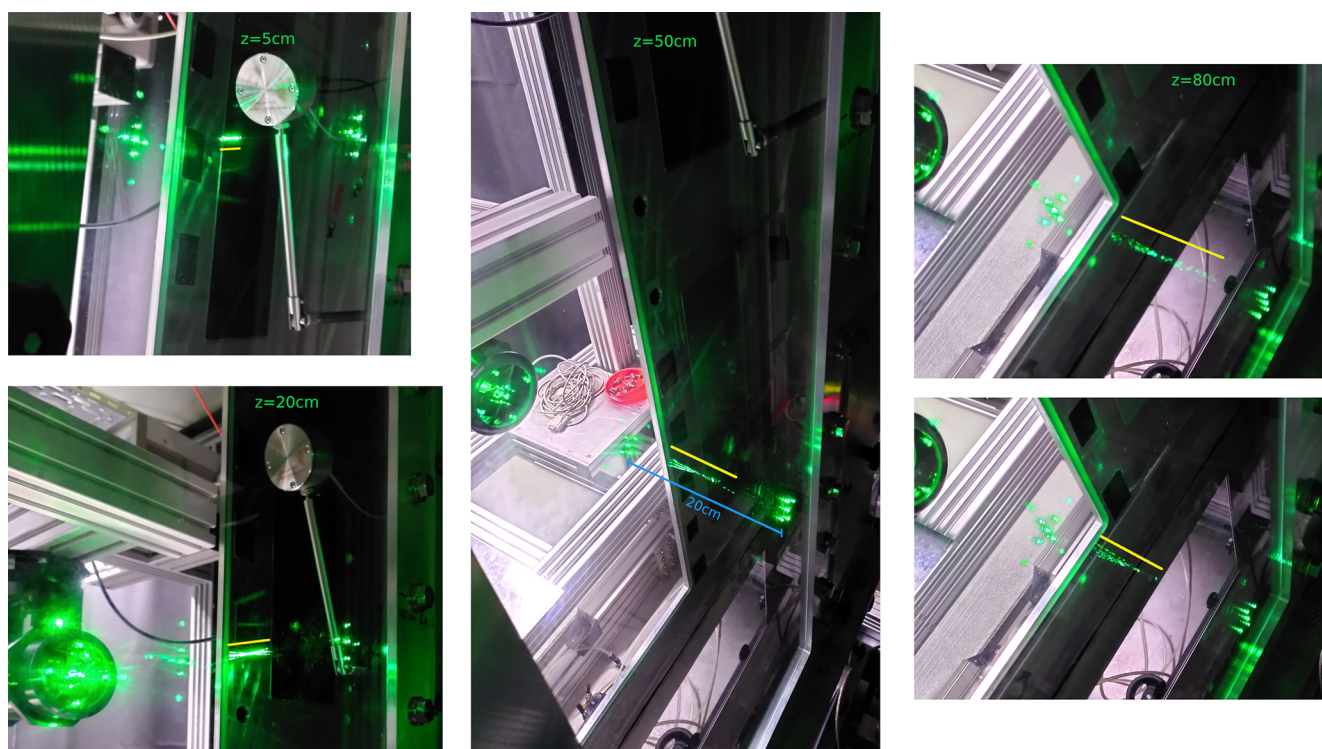
Figure 3. Pictures of the droplet stream taken at different z-positions (as indicated in the specific snapshots). The broadening of the stream is visible, as well as the very variable nature of the droplet stream when comparing the two snapshots at $z = 80$ cm on the right side. The green reflections of the laser light on the windows on either side can help the reader to estimate the dimensions, as the two windows are 20 cm apart (indicated by the blue line in the middle snapshot). The yellow lines indicate the widths of the droplet stream at each location.

that is also provided on the Eurochamp Data Centre data base. For the latter, variables included in the data files are specified. For completeness, laboratory conditions are provided in Appendix B.

4.1 General observations

4.1.1 Temperature and dewpoint

During the experiments, the temperature inside the wind tunnel was measured with Pt100 sensors. To avoid disturbance of the flow in the middle of the air streams, only short sensors were used at either side with sensor heads at about 2 cm away from the walls. This means that wall effects had an influence on the temperature measurements in stream A and B and thus, temperatures observed by the Pt100 sensors do not represent the temperature in the middle of the respective air stream. The sensor which measured in the mixing zone was not affected by wall effects and thus resembles the temperature in the mixing plane. Comparison measurements with short and long Pt100 sensors from previous experiments have shown that the temperatures inside the air streams are generally well representing the set temperatures at the thermostats (see Niedermeier et al., 2020, for details). As the water droplets are injected into the middle of the measurement section, they will not be affected by wall heating influence. Under the light that there were only minor changes in temperature in the laboratory during the day, the temperature measurements with the short sensors nevertheless can be useful to identify whether the general temperature in the wind tunnel is stable. An example of the temperature measurements is shown in Fig. 4 for the observations taken on the 2 March 2022.

4.1.2 Flow speed

The flow speed in LACIS-T was measured by the vane anemometer before the installation of the droplet generator. Simultaneous measurements have not been possible due to positioning constraints of the anemometer and droplet generator: With the vane anemometer positioned above the droplet generator, the flow downstream of the anemometer would be disturbed, positioning below the droplet generator would mean that droplets hit the vane anemometer during measurements, disturbing those. The vane anemometer is moved from the middle of stream A to the middle of the y axis of LACIS-T (i.e. the mixing plane) to the middle of stream B, and in the vertical positioned at about 25 cm below the top of the measurement section. Sample times of the vane anemometer are at least 10 min per position and condition.
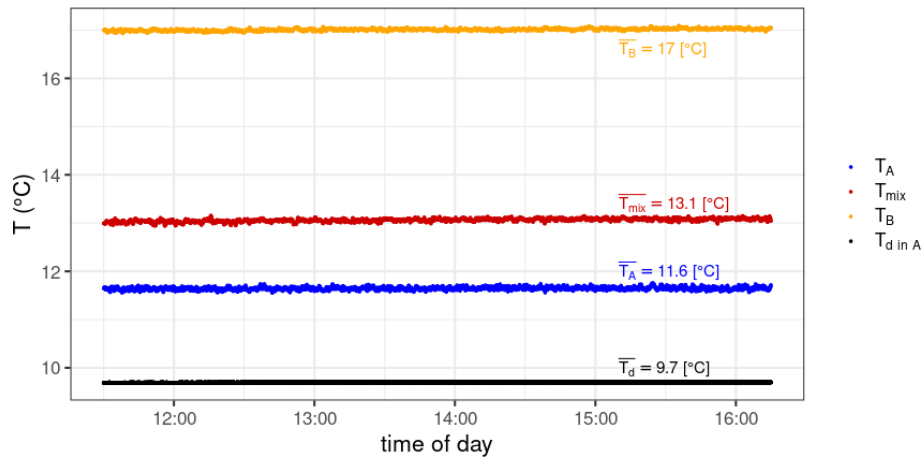
Figure 4. Temperatures as observed in LACIS-T on 2 March 2022, when the temperature in the laboratory was between 24.5 and 25.0 °C. Blue and yellow lines represent the temperature close to the walls in the streams A and B, respectively, red shows the temperature in the mixing zone between the two streams. The black line shows the dew point observed in stream A.
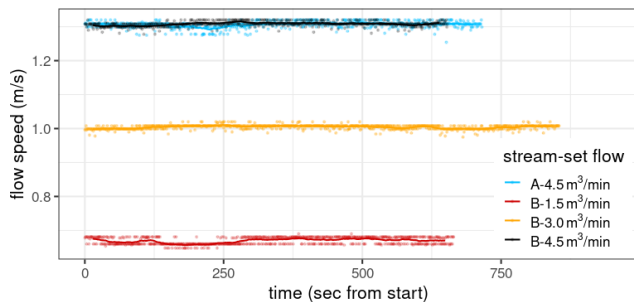
Figure 5. Flow speed measurements with the vane anemometer inside LACIS-T. Dots denote the 1 Hz observations, lines a 30 s running mean, set speed and respective air stream are indicated by the colours. The vane anemometer was positioned about 25 cm below the top of the measurement section.

Figure 5 show exemplary measurements of the flow speed in channel A and B of LACIS-T, in conditions as used during the main experiments. Table 1 provides the mean flow speeds as measured for the respective settings and their standard deviations.

4.1.3 Turbulence characteristics

Measurements of fluctuations to determine the turbulence statistics of the flow are unfortunately unavailable for this set of measurements. However, turbulence characteristics of LACIS-T based on observations (and simulations) are described in Niedermeier et al. (2020), who have also shown that the OpenFOAM setup is able to reproduce the characteristics in its simulations. Thus, we provide some information on the simulated turbulence characteristics in Sect. 5.2.

Table 1. Mean flow speeds as measured by the vane anemometer (middle column) for a given flow rate setting (left column, colour as in Fig. 5), and the respective standard deviation (SD, right column) as corresponding to the measurements shown in Fig. 5.

Flow set (channel) $(m^3\,min^{-1})$	Flow meas $(m\,s^{-1})$	SD
4.5 (A)	1.31	0.01
1.5 (B)	0.67	0.011
3.0 (B)	1.0	0.006
4.5 (B)	1.31	0.007

4.2 Particle observations

The cloud droplets in LACIS-T were observed at varying positions by the PDA system. Two types of particle data files are provided in the data set: (1) size distributions for each measurement position combined into one file, (2) single particle data for each position. The single particle data provided include the time stamp of the individual particles, their residence time within the PDA measuring volume, their velocity in z-direction, and their diameter. There is one data file for each measurement position and all measurements were obtained in the middle of the droplet stream. The size distribution file provides one size distribution for each measurement position in the form of $dN/dlog D_p$, averaged over the respective single particle file. Furthermore, it provides the particle counts per bin (n) and the bin sizes. The sample volume of the PDA is defined by the intersection of the two incident laser beams and is shaped as an ellipsoid with the two diameters $d_1 = 0.05122$ and $d_2 = 0.4237$ mm. The sample volume is then calculated using the mean particle velocity $\overline{v}_p$ and the sample time t_s (see Sect. 3 and Appendix A):

$SV = \pi \frac{d_1}{2} \frac{d_2}{2} t_s \overline{v}_p$. An example of size distribution measurements can be seen in Fig. 6. The distance to the droplet generator can be associated with the mean residence time of the droplets in the turbulent environment. Thus, the further away from the droplet generator, the longer the residence time.

The mean Stokes numbers for the droplets are for all settings < 0.053, calculated following Devenish et al. (2012), using the measurements to retrieve the droplet characteristic inertial response time, and the simulations for retrieving the Kolmogorov timescale.

5   Model setup and output

In order to help to analyse and interpret the measurement data, the Computational Fluid Dynamics (CFD) model package OpenFOAM is employed in a LACIS-T setup, simulating multi-region heat and mass transport. It has already been used successfully for studying cloud processes observed in LACIS-T, as droplet activation and growth, and entrainment (see description in Niedermeier et al., 2020). OpenFOAM allows for the numerical solution of small-scale processes by solving the transient, compressible Navier-Stokes-Equations on a fine (mm-scale) grid for the domain of the LACIS-T chamber. For simulations of non-isothermal and humidified flows, an adapted version of OpenFOAM's "chtMultiRegionFoam" solver is employed, which solves the conservation equations for mass, momentum, energy, and water vapour content. Turbulence is simulated using the dynamic k-equation Large Eddy Simulation (LES) model. For further details see Niedermeier et al. (2020). To simulate particle (i.e. cloud droplets) dynamics, an Euler-Lagrange approach is used. This tracks individual particles along their trajectories through the simulation domain. Droplet growth (including Köhler theory) and evaporation are both resolved in the current model version, with a two way transport of water vapour between the fluid and particle phase. Additional growth by collision and coalescence and ice microphysics are not (yet) implemented. There are 20 000 particles released into the domain per model second, which roughly corresponds to the 100 000 particles observed during the shortest initial measurements at $z = 0$ cm that took about 5 s (see Table A1). The initial size distribution for the simulations is obtained from the measured size distribution at $z = 0$ cm on 2 March 2022, which is consistent for all experiment days (see Fig. 2), only the size distributions provided by the droplet generator on the 16 February 2022 diverged from this. Here, the size distribution showed a stronger bimodality. Nevertheless, the same size distribution has been used in all model simulation setups, to allow for direct comparisons. The model input size distribution has been obtained from a curve fit and cut for values below 13.5 μm and above 23.5 μm. Initial and final size distributions at the measurement position $z = 0$ cm and the fitted size distribution are shown in Fig. 2, using the fit function as specified in Eq. (1), with the droplet diameter D_p, mode

mean diameter $\overline{D}_p$, standard deviation σ, and weight w, and the subscript denoting the mode of the size distribution. The figure further indicates the obtained fit function values.

$$f(D_p) = w_1 \frac{1}{\sqrt{2\pi}\sigma_1} \exp^{-(D_p - \overline{D}_{p_1})^2 / 2\sigma_1^2}$$
$$+ w_2 \frac{1}{\sqrt{2\pi}\sigma_2} \exp^{-(D_p - \overline{D}_{p_2})^2 / 2\sigma_2^2} \quad (1)$$

The initial simulated particle count distributions compare well to the respective observations. Differences arise when comparing OpenFOAM and observed size distributions using concentrations ($dN/d\log D_p$), possibly due to differences between simulation and experiment in terms of the injection properties and sampling areas (see more details in Appendix C). Model simulations are run for all three flow settings (no shear/low shear/high shear) resembling the measurements on the 16 February and 1 and 2 March 2022. One additional simulation for the no shear case was run, where a slight deviation of 0.05 m s^{-1} was imposed on the flow speed in channel B, to identify whether a potential deviation in flow speed during the measurements would have a noticeable effect on the turbulence characteristics and potentially on the droplet size distributions.

5.1   Particle data

In order to save resources, not the complete particle trajectories are stored, but only particle properties at specified levels (planes) in the model domain. These levels are set to coincide with the measurement locations at $z = 0$ cm, $z = 5$ cm, $z = 20$ cm, and $z = 50$ cm. The $z = 80$ cm level is located outside the model domain, as it was kept shorter due to computing costs. The simulated particle properties include the x, y, and z position of the particle, 3D particle velocity, RH and temperature at particle location, particle diameter, and particle mass. It has to be noted that there is a strong deviation of the simulated size distributions to the observed size distributions (simulated particles decrease in size too fast). Possible causes could be that the droplet generator geometry is not included in the model domain setup, and thus, the resulting disturbances in the flow field are absent from the simulations, and secondly, additional growth processes (other than diffusional growth) are not resolved in the model, like e.g. the process of collision and coalescence and thus, potential particle growth is not simulated. Particularly for the size distributions close to the droplet generator head, where additionally the particle number concentrations are high, we believe that the combination of these effects leads to the deviation between simulated and observed droplet size distributions. Therefore, the simulated particle data are not stored with the other data in the data base of the Eurochamp Data Centre. However, the data can be obtained from the authors upon request. The simulated size distributions are shown for completeness in Appendix C.
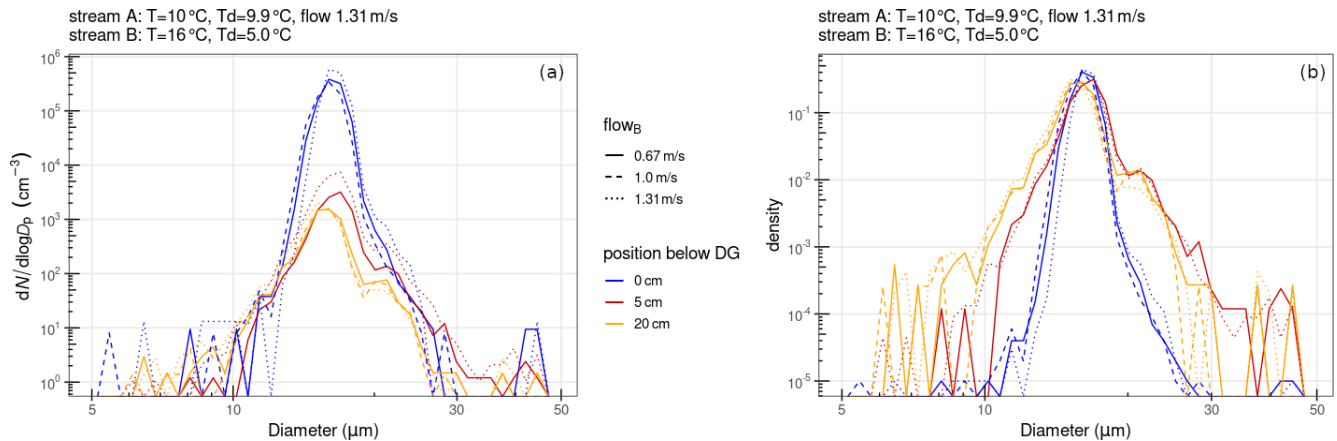
Figure 6. Size distributions as observed in LACIS-T on 23 February 2022, with different flow speeds in stream B (denoted by different line strokes), for the upper positions of the PDA system. The varied flow speed does not seem to have a large impact on the size distributions, while with increased residence time of the particles (i.e. increased distance to the droplet generator) a broadening of the size distributions can be seen. The left panel **(a)** shows the size distributions with $\mathrm{d}N/\mathrm{dlog}D_\mathrm{p}$, while the right panel **(b)** displays the size distributions normalised by total counts of droplets.

5.2 Conditions in the wind tunnel and turbulence data

The model data file provides general conditions in the middle of the $x-y$ plane on several levels. Note, that $z_\mathrm{M} = 0\,\mathrm{cm}$ in the model file corresponds to the top of the simulated measurement section, not to the position of the droplet generator, which is located at $z_\mathrm{M} = 35\,\mathrm{cm}$. As mentioned above, the levels for the model data output coincide with the droplet measurement positions as far as possible, plus some additional levels in between are specified. Thus, model data are provided for $z_\mathrm{M} = 1$, $z_\mathrm{M} = 35$, $z_\mathrm{M} = 40$, $z_\mathrm{M} = 55$, $z_\mathrm{M} = 70$, $z_\mathrm{M} = 85\,\mathrm{cm}$. The data start at 1 s into the simulation, to allow enough spinup time of the model and furthermore, the particles are also released into the model domain from 1 s on. The data contain for each location: temperature, relative humidity, absolute humidity, velocity in all three directions (w pointing downwards/along the LACIS-T general flow), turbulent kinetic energy, and eddy dissipation rate. Figure 7 shows some of the simulated turbulence statistics (eddy dissipation rate (ϵ), turbulent kinetic energy (TKE), Taylor microscale, and Taylor Reynolds number) in the mixing plane of LACIS-T.

6 Data availability

The data sets are available at the Database of Atmospheric Simulation Chamber Studies at the AC-TRIS/Eurochamp2020 Data Centre (experiment type "cloud study", https://data.eurochamp.org/data-access/chamber-experiments/#/, last access: 20 March 2026). There is one data set for each experiment day and flow speed as specified in Table 2.

7 Future use – examples

As stated by Morrison et al. (2020), laboratory work is supposed to be essential to improve our understanding of cloud microphysical processes. Thus, the data set presented here provides an important data set for furthering our knowledge and can be used to study several processes regarding cloud microphysics in turbulent environments. Some examples of such processes are elaborated below:

– *Collision and coalescence.* The size distributions observed are not only showing a broadening towards smaller but also towards larger sizes (cf. Fig. 6). As residence times of the droplets are too short to allow condensational growth to those sizes (in the given time), this growth might be attributed to collision and coalescence. It has to be noted that changes in the size distributions between $z = 0\,\mathrm{cm}$ and $z = 5\,\mathrm{cm}$ are most likely strongly influenced by the droplet generator head and the conditions created by it (e.g. disturbances of the flow field and high velocities of droplets and focussing air exiting the droplet generator). Additionally, collisions within the first centimetres are enhanced by the high droplet number concentrations created by the droplet generator. Further experiments in LACIS-T studying particle growth are planned, which will also more closely study the influence of the droplet generator on the flow field, using the data described here as a test bed.

– *Entrainment/cloud-clear interface.* Mixing in this experiment setup happens between the droplet stream and cloud free air. Thus, the data could be used for investigating entrainment, or mixing at the cloud/clear interface.
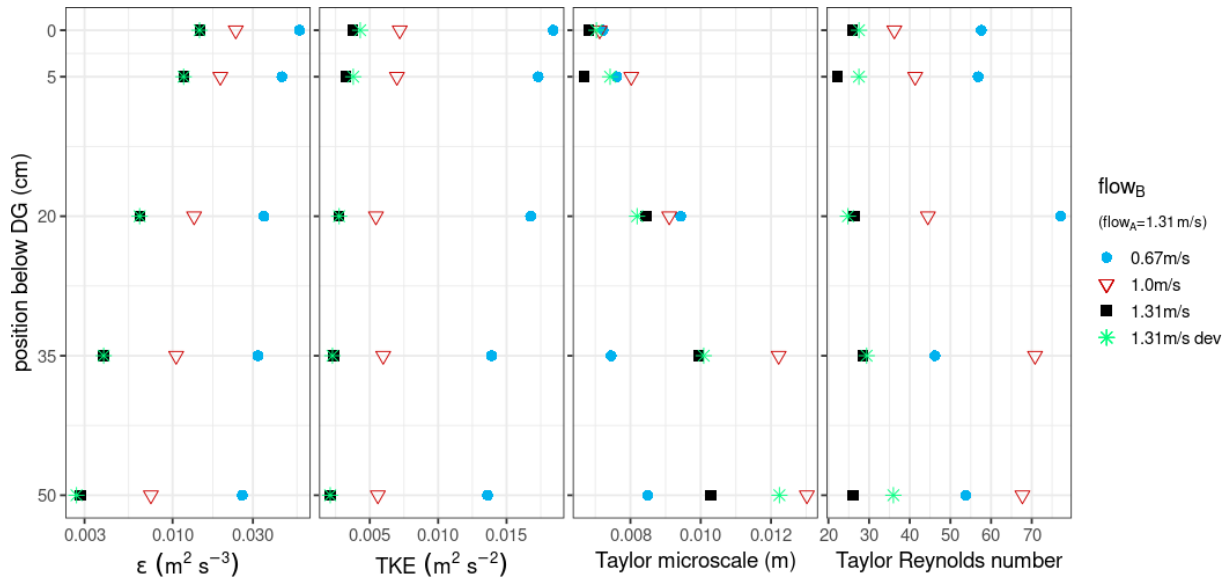
Figure 7. Turbulence statistics versus position below the droplet generator as simulated with OpenFOAM, from left to right: eddy dissipation rate (ϵ), turbulent kinetic energy (TKE), Taylor microscale, and Taylor Reynolds number. Different colours and symbols denote the different flow settings.

Table 2. Data sets available from STEP project.

Date	Flow set (channel B) ($m^3 min^{-1}$)	DOI	Reference
16 Feb 2022*	4.5	https://doi.org/10.25326/3F1J-GQ35	Frey (2025a)
21 Feb 2022	3.0	https://doi.org/10.25326/M1AE-G137	Frey (2025c)
21 Feb 2022	1.5	https://doi.org/10.25326/6M2H-VC29	Frey (2025b)
22 Feb 2022	1.5	https://doi.org/10.25326/6WVK-9153	Frey (2025d)
23 Feb 2022*	4.5	https://doi.org/10.25326/CATS-D655	Frey (2025g)
23 Feb 2022	3.0	https://doi.org/10.25326/SV3H-CV11	Frey (2025f)
23 Feb 2022	1.5	https://doi.org/10.25326/BT77-NA95	Frey (2025e)
1 Mar 2022*	3.0	https://doi.org/10.25326/T0TG-VV79	Frey (2025h)
2 Mar 2022*	1.5	https://doi.org/10.25326/1F17-VZ46	Frey (2025i)

* denotes data sets that include model simulation data.

– *Fundamental processes – mixing.* More broadly speaking, the data set could be used for mixing studies, where one would investigate the respective contribution of homogeneous versus inhomogeneous mixing.

– *Clustering.* A further potential use could be to study cloud clustering, by looking at the single particle data and how they are distributed in the time space at one location.

– *Effect/impact of shear.* Even though the strength of the shear flow does not seem to have a (significant) impact on the size distributions (cf. Fig. 6), the data set offers the possibility to look at shear effects more closely, also in connection with the simulation data.

Overall, we present rare laboratory data of cloud droplets in a turbulent environment. Thus, we believe that this data will not only be useful for studying processes as outlined above, but will also be useful as a test bed for several model studies, both on individual level and for model inter-comparison projects. Additionally, it can be used to validate simulations.

Appendix A: Data availability and sample times

Table A1 gives an overview of all conducted experiments, including the sample times for each measurement.

Table A1. Data availability overview: an x in the flow rate columns indicates at what flow rate ($m^3 min^{-1}$) the measurements were taken (as "flow in stream A – flow in stream B"), the numbers in the z-position columns indicate the measurement sample time in seconds, note that for $z = 0$ cm (start and end) the observations were stopped when the particle count reached 100 000 (except for measurements on the 16 and 21 February 2022, where the particle count threshold was 1 000 000).

date	flow rate A–B ($m^3 min^{-1}$)			z-position (cm)					
	4.5–4.5	4.5–3.0	4.5–1.5	0 (start)	5	20	50	80	0 (end)
16 Feb 2022	x			300 s	300 s		300 s	600 s	
21 Feb 2022		x		55 s				600 s	
21 Feb 2022			x				600 s	600 s	60 s
22 Feb 2022			x	4.6 s	600 s		600 s	600 s	14.7 s
23 Feb 2022	x			5.7 s	600 s	600 s			
23 Feb 2022		x		9.7 s		600 s			
23 Feb 2022			x	8.2 s	600 s	600 s			
1 Mar 2022		x		17.4 s	300 s	300 s	600 s	600 s	7.3 s
2 Mar 2022			x	7.7 s	300 s	300 s	600 s	600 s	11.1 s

Appendix B: Laboratory conditions

Laboratory conditions are noted at the beginning and the end of a measurement day, in terms of pressure, temperature, and dew point. As LACIS-T is not sealed, strong pressure perturbations in the laboratory would also intrude into the wind tunnel. Strong temperature perturbations might impact the temperature stability in the wind tunnel closer to the walls, no effects are expected towards the middle of the measurement section, due to the constant air flow. However, strong changes in laboratory conditions were not observed for the measurements presented here, as can be seen in Table B1.

Table B1. Conditions in the laboratory at the start and end of the measurement days. For each day, pressure p, temperature T, and dewpoint T_d are noted at the begin and end of day, as well as the used flow conditions in the air stream with the variable flow rate.

| date	flow$_B$ ($m^3 min^{-1}$)	begin of day			end of day		
		p (hPa)	T (°C)	T_d (°C)	p (hPa)	T (°C)	T_d (°C)
16 Feb 2022	4.5	989.7	23.8	1.6	983.4	23.6	3.1
21 Feb 2022	1.5/3.0	985.2	25.1	−0.8	982.9	25.3	−3.2
22 Feb 2022	1.5	1002.2	25.4	−0.7	1001.8	25.3	−1.7
23 Feb 2022	1.5/3.0/4.5	1010.6	25.5	0.3	1010.8	25.8	−1.0
1 Mar 2022	3.0	1017.7	25.3	−10.8	1015.8	25.1	−8.4
2 Mar 2022	1.5	1011.9	24.5	−6.0	1009.7	25.0	−7.5

Appendix C: Simulated size distributions

Comparing the simulated and observed particle count distribution for the high shear experiment (2 March 2022) the initial size distributions (blue lines) compare relatively well, see Fig. C1a. Some deviation is visible, caused by observed particles that lie outside the size range of the injected simulated particles. Nevertheless, when comparing OpenFOAM and observed size distributions plotted as $dN/d\log D_p$ (Fig. C1b), the peak in the initial OpenFOAM size distribution
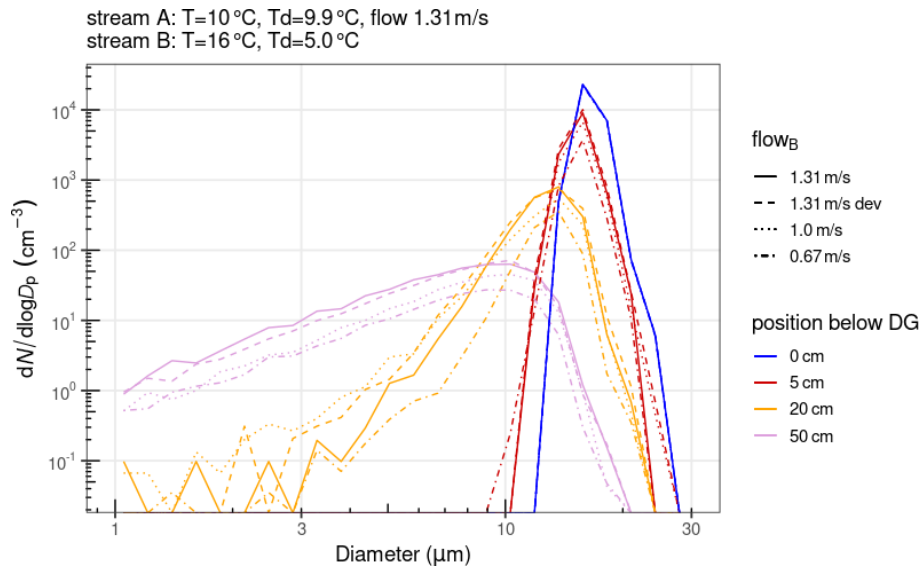
is about a factor of 5 lower than the peak at $z = 0$ cm of the observed size distribution (the figures show a similar behaviour for the low and no shear experiments). In the present OpenFOAM model, particles are injected at specified grid cells, which makes it difficult to exactly match the injection regions of the experiment in the simulation, as the nozzle outlet is smaller than the model's grid cells. Furthermore, it is difficult to match the sample areas in OpenFOAM and the

experiment, as the horizontal cross section of the PDA measurement volume is only on the order of the cross section of a grid cell. Also, the injection rate and size distribution of droplets is not actually known but derived from the point measurements with the PDA, which may introduce further errors. Further downstream the spray nozzle this is less of an issue as the droplet spray widens up and the sample area just covers a part of the area that the droplet stream would cover on that respective level. Here, deviations in droplet sizes start playing a larger role: The simulated particles (partially) evaporate and thus decrease in size too quickly, which causes a too strong shift of the peak sizes to the smaller sizes when moving further downstream. We ran an additional simulation in order to see whether we could achieve a better match in (a) peak concentrations and (b) peak sizes by using a higher number of injected particles (150 000 instead of 20 000 particles per second). The decrease of particle sizes was not as strong as in the 20 000 particles/second case (more particles lead to more evaporation releasing humidity back into the flow), still the peak sizes decreased in size too much, while the particle concentrations were much too high. At the same time, the high amount of particles released into the domain increased the computing time significantly, and therefore, we chose to keep the injection numbers at 20 000, as this number compared well in the particle count distributions.

All simulated size distributions for the three different flow settings as used during the experiments on 16 February, 1 and 2 March 2022 are shown in Fig. C2, also including the additional simulation for the same flow experiment (16 February 2022) with the slight flow speed deviation.
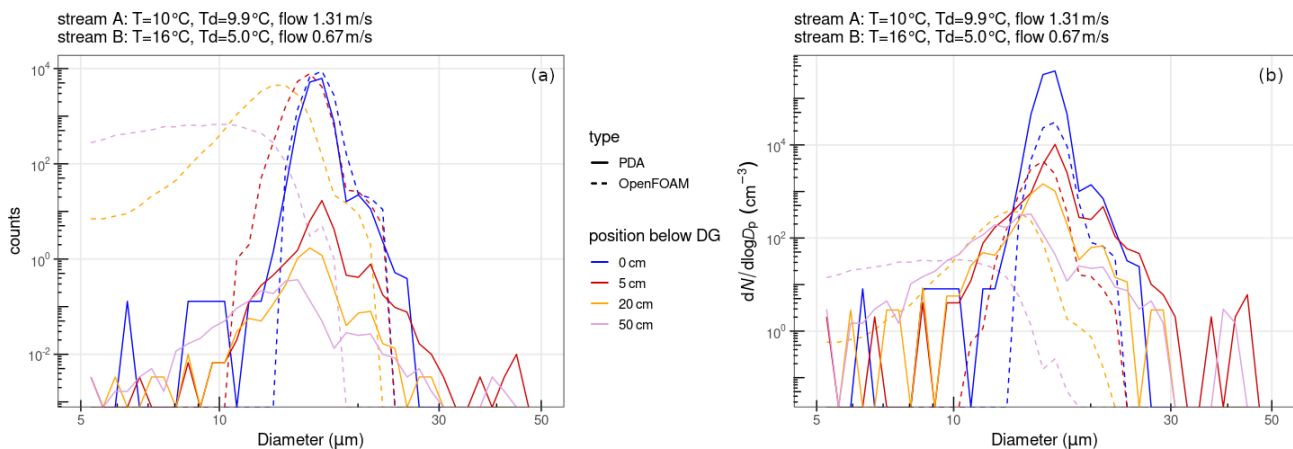
Figure C1. Comparison of particle distributions measured by the PDA (solid lines) and simulated by OpenFOAM (dashed lines) for the high shear flow experiment within one second. Colours indicate the position below the droplet generator. The left panel **(a)** shows the particle count distributions, the right panel shows the size distributions with $\mathrm{d}N/\mathrm{d}\log D_\mathrm{p}$.

https://doi.org/10.5194/essd-18-2305-2026

Earth Syst. Sci. Data, 18, 2305–2318, 2026

Figure C2. Simulated size distributions for all flow setting used during the experiments (and one sensitivity on small flow deviation), sampled at the same locations downstream the droplet generator as in the experiments. The size distribution at $z = 80$ cm is located outside the model domain, and thus, not simulated.

Competing interests. The contact author has declared that none of the authors has any competing interests.

Disclaimer. Publisher's note: Copernicus Publications remains neutral with regard to jurisdictional claims made in the text, published maps, institutional affiliations, or any other geographical representation in this paper. The authors bear the ultimate responsibility for providing appropriate place names. Views expressed in the text are those of the authors and do not necessarily reflect the views of the publisher.

References

Allwayin, N., Larsen, M. L., Glienke, S., and Shaw, R. A.: Locally narrow droplet size distributions are ubiquitous in stratocumulus clouds, Science, 384, 528–532, https://doi.org/10.1126/science.adi5550, 2024.

Ayala, O., Rosa, B., Wang, L.-P., and Grabowski, W. W.: Effects of turbulence on the geometric collision rate of sedimenting droplets. Part 1. Results from direct numerical simulation, New J. Phys., 10, 075015, https://doi.org/10.1088/1367-2630/10/7/075015, 2008.

Bera, S., Prabha, T. V., and Grabowski, W. W.: Observations of monsoon convective cloud microphysics over India and role of entrainment-mixing, J. Geophys. Res.-Atmos., 121, 9767–9788, https://doi.org/10.1002/2016JD025133,2016.

Chandrakar, K. K., Cantrell, W., Chang, K., Ciochetto, D., Niedermeier, D., Ovchinnikov, M., Shaw, R. A., and Yang, F.: Aerosol indirect effect from turbulence-induced broadening of cloud-droplet size distributions, P. Natl. Acad. Sci. USA, 113, 14243–14248, https://doi.org/10.1073/pnas.1612686113, 2016.

Chandrakar, K. K., Grabowski, W. W., Morrison, H., and Bryan, G. H.: Impact of Entrainment Mixing and Turbulent Fluctuations on Droplet Size Distributions in a Cumu-

lus Cloud: An Investigation Using Lagrangian Microphysics with a Subgrid-Scale Model, J. Atmos. Sci., 78, 2983–3005, https://doi.org/10.1175/JAS-D-20-0281.1, 2021.

Chang, K., Bench, J., Brege, M., Cantrell, W., Chandrakar, K., Ciochetto, D., Mazzoleni, C., Mazzoleni, L. R., Niedermeier, D., and Shaw, R. A.: A Laboratory Facility to Study Gas-Aerosol-Cloud Interactions in a Turbulent Environment: The Π Chamber, B. Am. Meteorol. Soc., 97, 2343–2358, https://doi.org/10.1175/BAMS-D-15-00203.1, 2016.

Chen, S., Yau, M. K., and Bartello, P.: Turbulence Effects of Collision Efficiency and Broadening of Droplet Size Distribution in Cumulus Clouds, J. Atmos. Sci., 75, 203–217, https://doi.org/10.1175/JAS-D-17-0123.1, 2018.

Desai, N., Liu, Y., Glienke, S., Shaw, R. A., Lu, C., Wang, J., and Gao, S.: Vertical Variation of Turbulent Entrainment Mixing Processes in Marine Stratocumulus Clouds Using High-Resolution Digital Holography, J. Geophys. Res.-Atmos., 126, e2020JD033527, https://doi.org/10.1029/2020JD033527, 2021.

Devenish, B. J., Bartello, P., Brenguier, J.-L., Collins, L. R., Grabowski, W. W., IJzermans, R. H. A., Malinowski, S. P., Reeks, M. W., Vassilicos, J. C., Wang, L.-P., and Warhaft, Z.: Droplet growth in warm turbulent clouds, Q. J. Roy. Meteor. Soc., 138, 1401–1429, https://doi.org/10.1002/qj.1897, 2012.

D'Alessandro, J. J. and McFarquhar, G. M.: Impacts of Drop Clustering and Entrainment-Mixing on Mixed Phase Shallow Cloud Properties Over the Southern Ocean: Results From SOCRATES, J. Geophys. Res.-Atmos., 128, e2023JD038622, https://doi.org/10.1029/2023JD038622, 2023.

Frey, W.: Atmospheric simulation chamber study: water + None – Cloud study – 2022-02-16, ACTRIS [data set], https://doi.org/10.25326/3F1J-GQ35, 2025a.

Frey, W.: Atmospheric simulation chamber study: water + None – Cloud study – 2022-02-21, ACTRIS [data set], https://doi.org/10.25326/6M2H-VC29, 2025b.

Frey, W.: Atmospheric simulation chamber study: water + None – Cloud study – 2022-02-21, ACTRIS [data set], https://doi.org/10.25326/M1AE-G137, 2025c.

Frey, W.: Atmospheric simulation chamber study: water + None – Cloud study – 2022-02-22, ACTRIS [data set], https://doi.org/10.25326/6WVK-9153, 2025d.

Frey, W.: Atmospheric simulation chamber study: water + None – Cloud study – 2022-02-23, ACTRIS [data set], https://doi.org/10.25326/BT77-NA95, 2025e.

Frey, W.: Atmospheric simulation chamber study: water + None – Cloud study – 2022-02-23, ACTRIS [data set], https://doi.org/10.25326/SV3H-CV11, 2025f.

Frey, W.: Atmospheric simulation chamber study: water + None – Cloud study – 2022-02-23, ACTRIS [data set], https://doi.org/10.25326/CATS-D655, 2025g.

Frey, W.: Atmospheric simulation chamber study: water + None – Cloud study – 2022-03-01, ACTRIS [data set], https://doi.org/10.25326/T0TG-VV79, 2025h.

Frey, W.: Atmospheric simulation chamber study: water + None – Cloud study – 2022-03-02, ACTRIS [data set], https://doi.org/10.25326/1F17-VZ46, 2025i.

Grabowski, W. W. and Wang, L.-P.: Growth of Cloud Droplets in a Turbulent Environment, Annu. Rev. Fluid Mech., 45, 293–324, https://doi.org/10.1146/annurev-fluid-011212-140750, 2013.

Hoffmann, F. and Feingold, G.: Entrainment and Mixing in Stratocumulus: Effects of a New Explicit Subgrid-Scale Scheme for Large-Eddy Simulations with Particle-Based Microphysics, J. Atmos. Sci., 76, 1955–1973, https://doi.org/10.1175/JAS-D-18-0318.1, 2019.

Karpińska, K., Bodenschatz, J. F. E., Malinowski, S. P., Nowak, J. L., Risius, S., Schmeissner, T., Shaw, R. A., Siebert, H., Xi, H., Xu, H., and Bodenschatz, E.: Turbulence-induced cloud voids: observation and interpretation, Atmos. Chem. Phys., 19, 4991–5003, https://doi.org/10.5194/acp-19-4991-2019, 2019.

Khain, A., Pinsky, M., Elperin, T., Kleeorin, N., Rogachevskii, I., and Kostinski, A.: Critical comments to results of investigations of drop collisions in turbulent clouds, Atmos. Res., 86, 1–20, https://doi.org/10.1016/j.atmosres.2007.05.003, 2007.

Klein, S. A. and Hall, A.: Emergent Constraints for Cloud Feedbacks, Current Climate Change Reports, 1, 276–287, https://doi.org/10.1007/s40641-015-0027-1, 2015.

Klocke, D., Pincus, R., and Quaas, J.: On Constraining Estimates of Climate Sensitivity with Present-Day Observations through Model Weighting, J. Climate, 24, 6092–6099, https://doi.org/10.1175/2011JCLI4193.1, 2011.

Kumar, B., Schumacher, J., and Shaw, R. A.: Cloud microphysical effects of turbulent mixing and entrainment, Theor. Comp. Fluid Dyn., 27, 361–376, https://doi.org/10.1007/s00162-012-0272-z, 2013.

Lasher-Trapp, S. G., Cooper, W. A., and Blyth, A. M.: Broadening of droplet size distributions from entrainment and mixing in a cumulus cloud, Q. J. Roy. Meteor. Soc., 131, 195–220, https://doi.org/10.1256/qj.03.199, 2005.

Lehmann, K., Siebert, H., and Shaw, R. A.: Homogeneous and Inhomogeneous Mixing in Cumulus Clouds: Dependence on Local Turbulence Structure, J. Atmos. Sci., 66, 3641–3659, https://doi.org/10.1175/2009JAS3012.1, 2009.

Lim, J.-S. and Hoffmann, F.: Between Broadening and Narrowing: How Mixing Affects the Width of the Droplet Size Distribution, J. Geophys. Res.-Atmos., 128, e2022JD037900, https://doi.org/10.1029/2022JD037900, 2023.

Lu, C., Sun, C., Liu, Y., Zhang, G. J., Lin, Y., Gao, W., Niu, S., Yin, Y., Qiu, Y., and Jin, L.: Observational Relationship Between Entrainment Rate and Environmental Relative Humidity and Implications for Convection Parameterization, Geophys. Res. Lett., 45, 13495–13504, https://doi.org/10.1029/2018GL080264, 2018.

Morrison, H., van Lier-Walqui, M., Fridlind, A. M., Grabowski, W. W., Harrington, J. Y., Hoose, C., Korolev, A., Kumjian, M. R., Milbrandt, J. A., Pawlowska, H., Posselt, D. J., Prat, O. P., Reimel, K. J., Shima, S.-I., van Diedenhoven, B., and Xue, L.: Confronting the Challenge of Modeling Cloud and Precipitation Microphysics, J. Adv. Model. Earth Sy., 12, e2019MS001689, https://doi.org/10.1029/2019MS001689, 2020.

Niedermeier, D., Voigtländer, J., Schmalfuß, S., Busch, D., Schumacher, J., Shaw, R. A., and Stratmann, F.: Characterization and first results from LACIS-T: a moist-air wind tunnel to study aerosol–cloud–turbulence interactions, Atmos. Meas. Tech., 13, 2015–2033, https://doi.org/10.5194/amt-13-2015-2020, 2020.

Niedermeier, D., Hoffmann, R., Schmalfuss, S., Frey, W., Senf, F., Hellmuth, O., Pöhlker, M., and Stratmann, F.: Particle deliquescence in a turbulent humidity field, Aerosol Res., 3, 219–230, https://doi.org/10.5194/ar-3-219-2025, 2025.

Onishi, R. and Seifert, A.: Reynolds-number dependence of turbulence enhancement on collision growth, Atmos. Chem. Phys., 16, 12441–12455, https://doi.org/10.5194/acp-16-12441-2016, 2016.

Sardina, G., Picano, F., Brandt, L., and Caballero, R.: Continuous Growth of Droplet Size Variance due to Condensation in Turbulent Clouds, Phys. Rev. Lett., 115, 184501, https://doi.org/10.1103/PhysRevLett.115.184501, 2015.

Saw, E.-W. and Meng, X.: Intricate relations among particle collision, relative motion and clustering in turbulent clouds: computational observation and theory, Atmos. Chem. Phys., 22, 3779–3788, https://doi.org/10.5194/acp-22-3779-2022, 2022.

Schlenczek, O., Nordsiek, F., Brunner, C. E., Chávez-Medina, V., Thiede, B., Bodenschatz, E., and Bagheri, G.: Airborne measurements of turbulence and cloud microphysics during PaCE 2022 using the Advanced Max Planck CloudKite Instrument (MPCK+), Earth Syst. Sci. Data Discuss. [preprint], https://doi.org/10.5194/essd-2025-112, in review, 2025.

Shaw, R. A.: Particle-turbulence interactions in atmospheric clouds, Annu. Rev. Fluid Mech., 35, 183–227, https://doi.org/10.1146/annurev.fluid.35.101101.161125, 2003.

Sherwood, S. C., Bony, S., and Dufresne, J.-L.: Spread in model climate sensitivity traced to atmospheric convective mixing, Nature, 505, 37–42, https://doi.org/10.1038/nature12829, 2014.

Siebert, H., Lehmann, K., Wendisch, M., Franke, H., Maser, R., Schell, D., Saw, E. W., and Shaw, R. A.: Probing Finescale Dynamics and Microphysics of Clouds with Helicopter-Borne Measurements, B. Am. Meteorol. Soc., 87, 1727–1738, https://doi.org/10.1175/BAMS-87-12-1727, 2006.

Siebert, H., Shaw, R. A., and Warhaft, Z.: Statistics of Small-Scale Velocity Fluctuations and Internal Intermittency in Marine Stratocumulus Clouds, J. Atmos. Sci., 67, 262–273, https://doi.org/10.1175/2009JAS3200.1, 2010.

Stevens, B., Bony, S., Farrell, D., Ament, F., Blyth, A., Fairall, C., Karstensen, J., Quinn, P. K., Speich, S., Acquistapace, C., Aemisegger, F., Albright, A. L., Bellenger, H., Bodenschatz, E., Caesar, K.-A., Chewitt-Lucas, R., de Boer, G., Delanoë, J., Denby, L., Ewald, F., Fildier, B., Forde, M., George, G., Gross, S., Hagen, M., Hausold, A., Heywood, K. J., Hirsch, L., Jacob, M., Jansen, F., Kinne, S., Klocke, D., Kölling, T., Konow, H., Lothon, M., Mohr, W., Naumann, A. K., Nuijens, L., Olivier, L., Pincus, R., Pöhlker, M., Reverdin, G., Roberts, G., Schnitt, S., Schulz, H., Siebesma, A. P., Stephan, C. C., Sullivan, P., Touzé-Peiffer, L., Vial, J., Vogel, R., Zuidema, P., Alexander, N., Alves, L., Arixi, S., Asmath, H., Bagheri, G., Baier, K., Bailey, A., Baranowski, D., Baron, A., Barrau, S., Barrett, P. A., Batier, F., Behrendt, A., Bendinger, A., Beucher, F., Bigorre, S., Blades, E., Blossey, P., Bock, O., Böing, S., Bosser, P., Bourras, D., Bouruet-Aubertot, P., Bower, K., Branellec, P., Branger, H., Brennek, M., Brewer, A., Brilouet , P.-E., Brügmann, B., Buehler, S. A., Burke, E., Burton, R., Calmer, R., Canonici, J.-C., Carton, X., Cato Jr., G., Charles, J. A., Chazette, P., Chen, Y., Chilinski, M. T., Choularton, T., Chuang, P., Clarke, S., Coe, H., Cornet, C., Coutris, P., Couvreux, F., Crewell, S., Cronin, T., Cui, Z., Cuypers, Y., Daley, A., Damerell, G. M., Dauhut, T., Deneke, H., Desbios, J.-P., Dörner, S., Donner, S., Douet, V., Drushka, K., Dütsch, M., Ehrlich, A., Emanuel, K., Emmanouilidis, A., Etienne, J.-C., Etienne-Leblanc, S., Faure, G., Feingold, G., Ferrero, L., Fix, A., Flamant, C., Flatau, P. J., Foltz, G. R., Forster, L.,

Furtuna, I., Gadian, A., Galewsky, J., Gallagher, M., Gallimore, P., Gaston, C., Gentemann, C., Geyskens, N., Giez, A., Gollop, J., Gouirand, I., Gourbeyre, C., de Graaf, D., de Groot, G. E., Grosz, R., Güttler, J., Gutleben, M., Hall, K., Harris, G., Helfer, K. C., Henze, D., Herbert, C., Holanda, B., Ibanez-Landeta, A., Intrieri, J., Iyer, S., Julien, F., Kalesse, H., Kazil, J., Kellman, A., Kidane, A. T., Kirchner, U., Klingebiel, M., Körner, M., Kremper, L. A., Kretzschmar, J., Krüger, O., Kumala, W., Kurz, A., L'Hégaret, P., Labaste, M., Lachlan-Cope, T., Laing, A., Landschützer, P., Lang, T., Lange, D., Lange, I., Laplace, C., Lavik, G., Laxenaire, R., Le Bihan, C., Leandro, M., Lefevre, N., Lena, M., Lenschow, D., Li, Q., Lloyd, G., Los, S., Losi, N., Lovell, O., Luneau, C., Makuch, P., Malinowski, S., Manta, G., Marinou, E., Marsden, N., Masson, S., Maury, N., Mayer, B., Mayers-Als, M., Mazel, C., McGeary, W., McWilliams, J. C., Mech, M., Mehlmann, M., Meroni, A. N., Mieslinger, T., Minikin, A., Minnett, P., Möller, G., Morfa Avalos, Y., Muller, C., Musat, I., Napoli, A., Neuberger, A., Noisel, C., Noone, D., Nordsiek, F., Nowak, J. L., Oswald, L., Parker, D. J., Peck, C., Person, R., Philippi, M., Plueddemann, A., Pöhlker, C., Pörtge, V., Pöschl, U., Pologne, L., Posyniak, M., Prange, M., Quiñones Meléndez, E., Radtke, J., Ramage, K., Reimann, J., Renault, L., Reus, K., Reyes, A., Ribbe, J., Ringel, M., Ritschel, M., Rocha, C. B., Rochetin, N., Röttenbacher, J., Rollo, C., Royer, H., Sadoulet, P., Saffin, L., Sandiford, S., Sandu, I., Schäfer, M., Schemann, V., Schirmacher, I., Schlenczek, O., Schmidt, J., Schröder, M., Schwarzenboeck, A., Sealy, A., Senff, C. J., Serikov, I., Shohan, S., Siddle, E., Smirnov, A., Späth, F., Spooner, B., Stolla, M. K., Szkółka, W., de Szoeke, S. P., Tarot, S., Tetoni, E., Thompson, E., Thomson, J., Tomassini, L., Totems, J., Ubele, A. A., Villiger, L., von Arx, J., Wagner, T., Walther, A., Webber, B., Wendisch, M., Whitehall, S., Wiltshire, A., Wing, A. A., Wirth, M., Wiskandt, J., Wolf, K., Worbes, L., Wright, E., Wulfmeyer, V., Young, S., Zhang, C., Zhang, D., Ziemen, F., Zinner, T., and Zöger, M.: EUREC[4]A, Earth Syst. Sci. Data, 13, 4067–4119, https://doi.org/10.5194/essd-13-4067-2021, 2021.

Tölle, M. H. and Krueger, S. K.: Effects of entrainment and mixing on droplet size distributions in warm cumulus clouds, J. Adv. Model. Earth Sy., 6, 281–299, https://doi.org/10.1002/2012MS000209, 2014.

Vaillancourt, P. A., Yau, M. K., Bartello, P., and Grabowski, W. W.: Microscopic Approach to Cloud Droplet Growth by Condensation. Part II: Turbulence, Clustering, and Condensational Growth, J. Atmos. Sci., 59, 3421–3435, https://doi.org/10.1175/1520-0469(2002)059<3421:MATCDG>2.0.CO;2, 2002.

Wang, A., Ovchinnikov, M., Yang, F., Cantrell, W., Yeom, J., and Shaw, R. A.: The Dual Nature of Entrainment-Mixing Signatures Revealed through Large-Eddy Simulations of a Convection-Cloud Chamber, J. Atmos. Sci., 81, 2017–2039, https://doi.org/10.1175/JAS-D-24-0043.1, 2024.

Yeom, J. M., Helman, I., Prabhakaran, P., Anderson, J. C., Yang, F., Shaw, R. A., and Cantrell, W.: Cloud microphysical response to entrainment and mixing is locally inhomogeneous and globally homogeneous: Evidence from the lab, P. Natl. Acad. Sci. USA, 120, e2307354120, https://doi.org/10.1073/pnas.2307354120, 2023.